Optics Letters

Multimode-fiber-based single-shot full-field measurement of optical pulses

WEN XIONG, SHAI GERTLER, HASAN YILMAZ, AND HUI CAO*

Department of Applied Physics, Yale University, New Haven, Connecticut 06520, USA
*Corresponding author: hui.cao@yale.edu

Received 24 January 2020; revised 16 March 2020; accepted 17 March 2020; posted 17 March 2020 (Doc. ID 388616); published 15 April 2020

Multimode fibers are explored widely for optical communication, spectroscopy, imaging, and sensing applications. Here we demonstrate a single-shot full-field temporal measurement technique based on a multimode fiber. The complex spatiotemporal speckle field is created by a reference pulse propagating through the fiber, and it interferes with a signal pulse. From the time-integrated interference pattern, both the amplitude and the phase of the signal are retrieved. The simplicity and high sensitivity of our scheme illustrate the potential of multimode fibers as versatile and multi-functional sensors.

https://doi.org/10.1364/OL.388616

A multimode fiber (MMF) provides a versatile and multi-functional platform for communication [1], spectroscopy [2–4], imaging [5–9], and sensing applications [10–14]. Its abundant spatial degrees of freedom have been utilized for controlling spatial, temporal, spectral, or polarization states of transmitted light, making an MMF function as a microscope [5–9], a reconfigurable waveplate [15], or a pulse shaper [16–19]. The speckles, created by interference of multiple guided modes in an MMF, have been employed to detect changes in temperature, refractive index, and strain [10–13]. In optical coherence tomography (OCT), random temporal speckles created by MMFs have been used to image axial reflectivity profiles [20]. For spectroscopy application, the dependence of the output speckle pattern on the spectrum of an input signal has been utilized to transform an MMF into a compact and high-resolution spectrometer [2,3]. However, only the spectral amplitude can be extracted from the spatial intensity pattern, not the spectral phase, which is needed for full-field temporal measurement.

In this work, we propose and realize a novel method based on an MMF for single-shot full-field measurement of optical pulses. It utilizes the complex yet deterministic spatiotemporal speckle field $E(\mathbf{r}, t)$ produced by a reference pulse $f(t)$ propagating through an MMF. Such field $E(\mathbf{r}, t)$, which is two-dimensional (2D) in space $\mathbf{r}$ and one-dimensional (1D) in time t, interferes with the unknown field $g(t)$ of a signal pulse that is mutually coherent with $f(t)$. The interference pattern is integrated in time by a camera. From this pattern, both the spectral amplitude and the phase of the signal are retrieved. The Fourier transform gives the full field of $g(t)$. The temporal resolution δt is set by the temporal speckle size, which is inversely proportional to the spectral bandwidth of the reference pulse $\delta\omega$. The temporal range of a single-shot measurement, Δt, is set by the temporal length of the transmitted waveform, which is given by the inverse of the spectral correlation width $\Delta\omega$ of the MMF. A fiber with stronger modal dispersion has faster spectral decorrelation, thus covering a longer time window.

Our scheme can be considered as parallel ghost imaging in time. Compared to the conventional ghost imaging that relies on the sequential generation of different temporal waveforms [21], the MMF simultaneously creates many distinct temporal speckle patterns, each at a different spatial location of the output facet, to sample the signal. The parallel sampling enables single-shot measurement, eliminating the requirement for repetitive signals.

The proposed scheme is experimentally demonstrated in a Mach–Zehnder interferometric setup shown schematically in Fig. 1(a). A 230-fs-long pulse from a mode-locked near-IR fiber laser (NKT, Onefive Origami) is split by a beam splitter into two paths; one is launched into the MMF for creation of the spatiotemporal speckle field $E(\mathbf{r}, t)$, and the other is sent to probe a sample placed in the reference arm of the interferometer. The transmitted or reflected field $g(t)$ from the sample is combined with $E(\mathbf{r}, t)$ by a second beam splitter. Since the two fields are mutually coherent, they will interfere, as long as $g(t)$ overlaps with $E(\mathbf{r}, t)$ in time, which is ensured by matching the optical path lengths of the two arms of the interferometer. The time-integrated interference pattern is recorded by a camera (Xenics Xeva 1.7-640).

To increase the temporal length of $E(\mathbf{r}, t)$, which determines the measurement range, we adjust the launch condition for the reference pulse into the MMF so that it excites many guided modes that propagate at different speeds. Due to modal dispersion, the transmitted pulse is broadened and distorted. The pulse shape varies spatially across the fiber facet. To have strong modal dispersion, we choose a step-index fiber (105 μm core, 0.22 NA, Thorlabs FG105LCA) of 1.8-m length.

The spatiotemporal speckle at the fiber output can be calibrated in the time domain with the reference pulse of varying time delay (by scanning the length of the reference arm without a sample) [22]. Alternatively, the calibration can be done in the frequency domain by measuring the transmitted field profile

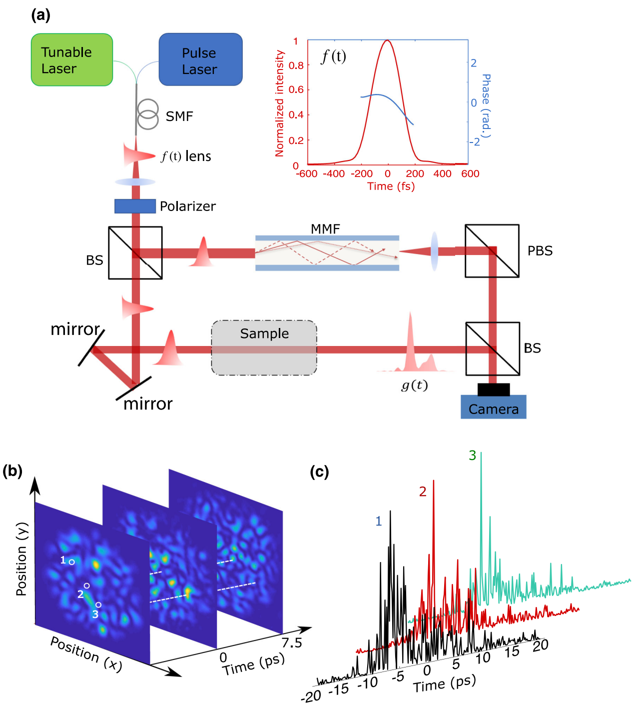

Fig. 1. Experimental setup and measured spatiotemporal speckles. (a) Schematic of a Mach–Zehnder interferometric setup for off-axis holography. Inset: intensity (red, solid) and phase (blue, solid) of the reference pulse launched into the MMF. BS, beam splitter; PBS, polarizing beam splitter. (b) Spatial field (amplitude) distribution of the laser pulse transmitted through the MMF at three arrival times −7.5, 0, and 7.5 ps. (c) Temporal field amplitudes at three spatial positions of the fiber output facet, marked by white circles in (b).

at each frequency. We perform the spectral calibration with a tunable continuous-wave (CW) fiber laser (Agilent 81940A). The laser wavelength λ is scanned from 1520 to 1570 nm with a step of 0.2 nm. This range fully covers the spectrum of the reference pulse, which is centered at $\lambda = 1546$ nm and has a full width at half maximum (FWHM) $\Delta\lambda = 12$ nm. To ensure the launch condition of the CW laser light into the MMF is identical to that of the pulsed laser, the outputs from both lasers are coupled into a single-mode fiber (SMF) switch. The amplitude and phase of the field transmitted through the MMF at a single frequency ω are extracted from the off-axis hologram, as described in Ref. [17]. By scanning the frequency ω of the CW laser, the frequency-resolved field transmission matrix $T(\mathbf{r}, \omega)$ is measured. At both the input and the output of the MMF, only one polarization is selected.

After calibrating $T(\mathbf{r}, \omega)$ of the MMF with the tunable CW laser, the input source is switched to a pulsed laser. The temporal intensity and phase of the reference pulse $f(t)$ are shown in the inset of Fig. 1(a). The Fourier transform of $f(t)$ is $F(\omega)$. The transmitted field of the MMF is $E(\mathbf{r}, \omega) = T(\mathbf{r}, \omega)F(\omega)$ in frequency, and $E(\mathbf{r}, t) = \mathcal{F}[E(\mathbf{r}, \omega)]$ in time. As shown in Fig. 1(b), the output speckle pattern changes rapidly in time. At each spatial location, the distinct temporal waveform is composed of multiple speckles, as plotted in Fig. 1(c).

The complex yet deterministic spatiotemporal speckles generated by the MMF enable single-shot full-field measurement of the unknown signal by interfering $E(\mathbf{r}, t)$ and $g(t)$. The time-integrated interference pattern is recorded by off-axis holography, $I(\mathbf{r}) = \int |E(\mathbf{r}, t) + g(t)|^2 \mathrm{d}t$. The information of $g(t)$ is encoded in the interference term $\tilde{I}(\mathbf{r}) = \int \mathrm{d}t[E(\mathbf{r}, t)g^*(t) + E^*(\mathbf{r}, t)g(t)]$, which is extracted by applying a Hilbert filter in the Fourier domain of the recorded interference pattern. The interference term can be expressed in the frequency domain as

$$\tilde{I}(\mathbf{r}) = \begin{bmatrix} T(\mathbf{r}, \omega)F(\omega) & T^*(\mathbf{r}, \omega)F^*(\omega) \end{bmatrix} \begin{bmatrix} G^*(\omega) \\ G(\omega) \end{bmatrix}, \quad \textbf{(1)}$$

where $G(\omega)$ is the Fourier transform of $g(t)$. With $T(\mathbf{r}, \omega)$ and $F(\omega)$ known, $G(\omega)$ is retrieved from $\tilde{I}(\mathbf{r})$ by an iterative optimization algorithm. The spatiotemporal speckle field is sampled by 251 points in real space and by 251 points in time/frequency, so that the number of linear equations is equal to the number of unknowns in (1). If $G(\omega)$ is sparse, more unknowns can be recovered from a fewer number of equations. We deploy a compressive sensing algorithm, FASTA [23], to solve the sparse least squares optimization problem.

To find the temporal resolution, we compute the temporal correlation function of the speckle field, $C(\Delta t) \equiv \langle E^*(\mathbf{r}, t)E(\mathbf{r}, t + \Delta t)\rangle$, where $\langle \ldots \rangle$ denotes averaging over $\mathbf{r}$ and t. The FWHM of $C(\Delta t)$ gives the average temporal speckle size $\delta t = 230$ fs, which determines the temporal resolution.

The temporal range of measurement Δt is equal to the temporal length of $E(\mathbf{r}, t)$, which is inversely proportional to the width of the spectral correlation function $C(\Delta\omega) \equiv \langle E^*(\mathbf{r}, \omega)E(\mathbf{r}, \omega + \Delta\omega)\rangle$. From the width of $C(\Delta\omega)$, we estimate Δt to be about 35 ps. The time bandwidth product (TBP), defined by the ratio of the temporal range to the temporal resolution, is $\Delta t/\delta t = 152$.

We first test our method by measuring single pulses propagating through the reference arm (without a sample) of the Mach–Zehnder interferometer with different delay times. We change the reference arm length with a delay line, and the arrival time τ of the pulse is 0 when the length of the reference arm matches that of the fiber arm. Figures 2(a) and 2(d) show the interference term $\tilde{I}(\mathbf{r})$ extracted from the experimentally measured hologram for two delay times $\tau = 0$ and 4 ps in these two cases. Although the pulse shape remains the same, the spatial interference pattern is very different. It is because pulses with varying delays interfere with different parts of the spatiotemporal speckles from the MMF. The recovered spectral intensity in Figs. 2(b) and 2(e) is consistent with the measurement using an optical spectral analyzer. While the recovered spectral phase is flat for $\tau = 0$ in Figs. 2(b), it changes linearly for $\tau = 4$ ps in Figs. 2(e). These results are expected, as the slope of the spectral phase corresponds to the delay time. In the time domain [Figs. 2(c) and 2(f)], the arrival times of the recovered pulses agree with the values set by the delay line, and the temporal pulse shape is consistent with the autocorrelation trace.

We next measure double pulses created by a double-side-polished silicon wafer in the reference arm of the Mach–Zehnder interferometer. The incident pulse is 2.2 ps long, obtained by spectral filtering the output from a mode-locked fiber laser (Calmar Mendocino). It is reflected back and forth between the two surfaces of the wafer, creating multiple pulses in transmission. In Fig. 3(a), the recovered spectral intensity (red solid line) exhibits a rapid oscillation, in good agreement with the simulated spectrum (black dotted line) using the transfer matrix method. The recovered spectral phase,

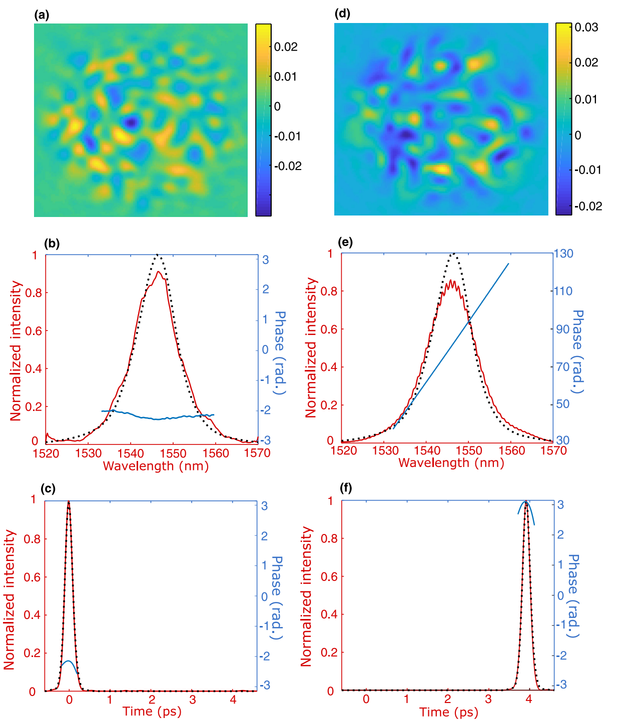

Fig. 2. Full-field measurement of single pulses with varying delay. (a), (d) 2D interference term $\tilde{I}(\mathbf{r})$ extracted from the off-axis hologram for a single pulse with arrival times $\tau = 0$ and 4 ps. (b), (e) Spectral intensity (red solid line, left axis) and spectral phase (blue solid line, right axis) of the signals retrieved from (a) and (d). The black dotted line is the spectral intensity of the signal measured by an optical spectrum analyzer. (c), (f) Temporal intensity (red solid line, left axis) and temporal phase (blue solid line, right axis) of the signals, obtained by a Fourier transform of (b) and (e), respectively. Black dotted line is the temporal intensity of the signal obtained from autocorrelation and spectrum measurements.

unwrapped and plotted by the blue solid line, features descending jumps at the frequencies of local minima for the spectral intensity. These phase jumps, together with the amplitude oscillations, are results of spectral interference of the double pulses shown in Fig. 3(b), which are reconstructed from the Fourier transform of the recovered spectral field in Fig. 3(a). The first pulse originates from direct transmission of the probe pulse through the wafer and the second pulse from two reflections within the wafer. They are spaced by 12.5 ps, which is consistent with the 3.75-mm-long one-round-trip optical path length in the silicon wafer. Because of the relatively low reflectivity of the silicon–air interface, the intensity ratio of the first pulse to the second pulse is 17.6. The temporal phases of the two pulses vary linearly, reflecting the absence of frequency chirp within each pulse.

Finally, we measure more complex pulses created by reflection from a thinner wafer. The interferometric setup is slightly modified to measure the pulses reflected by the sample in the reference arm. The Fourier transform of the recovered spectral field shown in Fig. 3(c) reveals three pulses in the time domain, as plotted in Fig. 3(d). The first pulse results from the direct reflection of the incident pulse by the front surface of the wafer, and the second pulse from direct reflection by the back surface. Even the third pulse, generated by three bounces in the wafer, is

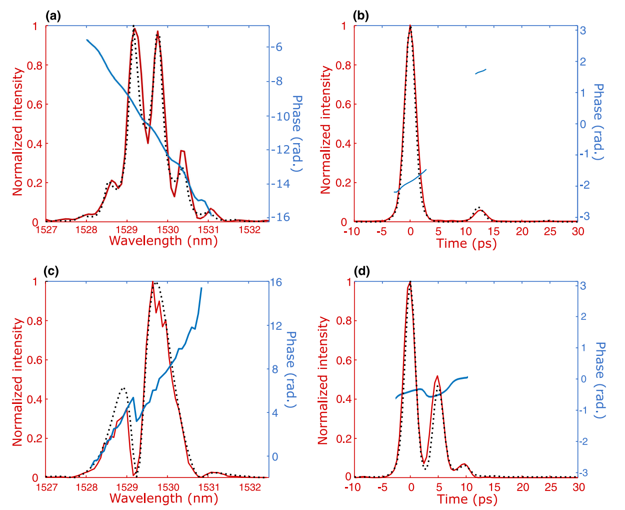

Fig. 3. Full-field measurement of multiple pulses. (a), (b) Transmission of the reference pulse through a silicon wafer of thickness 535 μm with an incident angle of 1°. (c), (d) Reflection of the reference pulse from a 212-μm-thick silicon wafer at an incident angle of 2°. Left column: spectral intensity (left axis) and spectral phase (right axis). Right column: temporal intensity (left axis) and temporal phase (right axis).

still visible and recovered in our measurement. Since this wafer is thinner than the previous one, the delay time between adjacent pulses is shortened to 5 ps, corresponding to one round-trip in this sample.

In summary, we demonstrate a novel MMF-based scheme for the single-shot full-field measurement of complex pulses. We obtain a temporal resolution of 230 fs, a temporal range of $\sim$35 ps, and a TBP of 152. The temporal resolution can be further enhanced by increasing the spectral bandwidth of the reference pulse. Using a 10-fs transform-limited pulse as the reference, the temporal resolution will reach 10 fs. If the pulse is not transform limited, its spectral bandwidth is broader and the temporal resolution will be finer. The temporal range of measurement is dictated by the spectral correlation width of the MMF, and scales linearly with the fiber length and the differential group delay. Using a 100-m-long MMF will increase the temporal range to 1 ns [3].

The temporal range of measurement is dictated by the spectral correlation width of the MMF and scales linearly with the fiber length and the differential group delay. The ratio of the temporal range to the temporal resolution, i.e., the TBP, gives the number of independent temporal channels that can be measured in a single shot. The upper limit of the TBP is bounded by the number of uncorrelated temporal traces at the MMF output facet, which is limited by the number of guided modes in the fiber, if there is no prior information on the signal. If there is, the TBP can exceed the number of fiber modes. For a fiber with a large core and a high numerical aperture, the TBP may well exceed 1000. However, if the core diameter is too large, the fiber becomes rigid ("light tube"), and its length is limited. Consequently, its temporal measurement range is narrower than that of a longer fiber that is flexible and can be coiled. Alternatively, the TBP may be increased by using coupled-core multi-core fibers or a bundle of smaller-core MMFs with longer lengths [24]. For example, the TBP can reach 10^5 with a bundle of 50 MMFs, each MMF having 2000 guided modes.

Taking full advantage of the complex spatiotemporal speckles created by the reference pulse through an MMF, our scheme eliminates the mechanical scanning of the time delay between the signal and the reference. While the spectral interferometry relies on a high-resolution grating spectrometer [25–31], our method is based on an MMF that can provide a higher spectral resolution [3] and thus a broader range of temporal measurement. Furthermore, the MMF has light weight and low cost and can be coiled to a small volume, compared to a high-resolution grating spectrometer. The high throughput of an MMF over a wide frequency range allows broadband operation of our method. Compared to other single-shot methods based on nonlinear processes such as time lenses [32–36], our scheme is based on linear interferometry, which possesses a much higher sensitivity. To avoid nonlinear mode coupling in the fiber, the reference pulse energy must be kept low; otherwise, the spatiotemporal speckle at the fiber output will depend on the input pulse energy, and the (linear) transmission matrix no longer works. For an MMF with a large core, it is possible to stay in the linear regime even for a temporal pulse shorter than 100 fs, as the pulse is stretched in both time and space, and the peak intensity is reduced [37].

With the knowledge of the reference pulse, as required by all linear interferometric methods [38], it can measure non-reproducible and non-periodic ultra-weak signals. The reference pulse is not necessarily transform limited, as long as its temporal or spectral amplitude and phase are known. Even without knowledge of the reference, the relative phase and amplitude change imposed by the sample can still be recovered. If $F(\omega)$ is not known, Eq. (1) can be rewritten as

$$\tilde{I}(\mathbf{r}) = \left[\, T(\mathbf{r},\omega) \;\; T^*(\mathbf{r},\omega) \,\right] \begin{bmatrix} F(\omega)G^*(\omega) \\ F^*(\omega)G(\omega) \end{bmatrix}. \tag{2}$$

From the measured interference pattern $\tilde{I}(\mathbf{r})$, $F^*(\omega)G(\omega)$ is recovered. Then we remove the sample from the reference arm of the interferometer and repeat the measurement to get $F^*(\omega)F(\omega)$. The ratio $F^*(\omega)G(\omega)/F^*(\omega)F(\omega) = G(\omega)/F(\omega) = H(\omega)$ gives the spectral response of the sample, and its Fourier transform gives the temporal response $h(t)$.

The simplicity and high sensitivity of our method illustrate the potential of MMFs as versatile and multi-functional sensors. To minimize external perturbations to the fiber that would require a frequent recalibration of its transmission matrix, the MMF can be housed in a temperature-controlled chamber [39]. Alternatively, the fiber may be replaced by a multimode waveguide fabricated in a silicon chip [40], which can be stabilized by a commercial temperature controller.

Funding. National Science Foundation (ECCS-1509361, ECCS-1809099).

Acknowledgment. The authors acknowledge Chia Wei Hsu, Yaniv Eliezer, and Logan Wright for fruitful discussions.

Disclosures. The authors declare no conflicts of interest.

REFERENCES

1. D. Richardson, J. Fini, and L. E. Nelson, Nat. Photonics **7**, 354 (2013).
2. B. Redding and H. Cao, Opt. Lett. **37**, 3384 (2012).
3. B. Redding, M. Alam, M. Seifert, and H. Cao, Optica **1**, 175 (2014).
4. G. C. Valley, G. A. Sefler, and T. J. Shaw, Opt. Lett. **41**, 2529 (2016).
5. I. N. Papadopoulos, S. Farahi, C. Moser, and D. Psaltis, Opt. Express **20**, 10583 (2012).
6. A. M. Caravaca-Aguirre, E. Niv, D. B. Conkey, and R. Piestun, Opt. Express **21**, 12881 (2013).
7. M. Plöschner, T. Tyc, and T. Čižmár, Nat. Photonics **9**, 529 (2015).
8. R. Y. Gu, R. N. Mahalati, and J. M. Kahn, Opt. Express **23**, 26905 (2015).
9. R. French, S. Gigan, and O. L. Muskens, Opt. Express **26**, 32302 (2018).
10. T. Okamoto and I. Yamaguchi, Appl. Opt. **27**, 3085 (1988).
11. Q. Wang and G. Farrell, Opt. Lett. **31**, 317 (2006).
12. Y. Liu and L. Wei, Appl. Opt. **46**, 2516 (2007).
13. E. Fujiwara, Y. T. Wu, and C. K. Suzuki, Opt. Laser Eng. **50**, 1726 (2012).
14. G. A. Sefler, T. J. Shaw, and G. C. Valley, Opt. express **26**, 21390 (2018).
15. W. Xiong, C. W. Hsu, Y. Bromberg, J. E. Antonio-Lopez, R. A. Correa, and H. Cao, Light Sci. Appl. **7**, 54 (2018).
16. J. Carpenter, B. J. Eggleton, and J. Schröder, Nat. Photonics **9**, 751 (2015).
17. W. Xiong, P. Ambichl, Y. Bromberg, B. Redding, S. Rotter, and H. Cao, Phys. Rev. Lett. **117**, 053901 (2016).
18. W. Xiong, P. Ambichl, Y. Bromberg, B. Redding, S. Rotter, and H. Cao, Opt. Express **25**, 2709 (2017).
19. P. Ambichl, W. Xiong, Y. Bromberg, B. Redding, H. Cao, and S. Rotter, Phys. Rev. X **7**, 041053 (2017).
20. S.-Y. Lee, P.-C. Hui, B. E. Bouma, and M. Villager, Opt. Express **28**, 1124 (2020).
21. P. Ryczkowski, M. Barbier, A. T. Friberg, J. M. Dudley, and G. Genty, Nat. Photonics **10**, 167 (2016).
22. R. Rokitski and S. Fainman, Opt. Express **11**, 1497 (2003).
23. T. Goldstein, C. Studer, and R. Baraniuk, "A field guide to forward-backward splitting with a FASTA implementation," arXiv:1411.3406 (2014).
24. S. F. Liew, B. Redding, M. A. Choma, H. D. Tagare, and H. Cao, Opt. Lett. **41**, 2029 (2016).
25. C. Froehly, A. Lacourt, and J. C. Vienot, J. Opt. **4**, 183 (1973).
26. L. Lepetit, G. Chériaux, and M. Joffre, J. Opt. Soc. Am. B **12**, 2467 (1995).
27. C. Dorrer, J. Opt. Soc. Am. B **16**, 1160 (1999).
28. C. Dorrer, N. Belabas, J.-P. Likforman, and M. Joffre, J. Opt. Soc. Am. B **17**, 1795 (2000).
29. R. Trebino, P. Bowlan, P. Gabolde, X. Gu, S. Akturk, and M. Kimmel, Laser Photon. Rev. **3**, 314 (2009).
30. J. Cohen, P. Bowlan, V. Chauhan, and R. Trebino, Opt. Express **18**, 6583 (2010).
31. J. Cohen, P. Bowlan, V. Chauhan, P. Vaughan, and R. Trebino, Opt. Commun. **284**, 3785 (2011).
32. C. Iaconis and I. A. Walmsley, Opt. Lett. **23**, 792 (1998).
33. P. O'shea, M. Kimmel, X. Gu, and R. Trebino, Opt. Lett. **26**, 932 (2001).
34. B. Li, S.-W. Huang, Y. Li, C. W. Wong, and K. K. Wong, Nat. Commun. **8**, 61 (2017).
35. P. Ryczkowski, M. Närhi, C. Billet, J.-M. Merolla, G. Genty, and J. M. Dudley, Nat. Photonics **12**, 221 (2018).
36. A. Tikan, S. Bielawski, C. Szwaj, S. Randoux, and P. Suret, Nat. Photonics **12**, 228 (2018).
37. Z. Liu, L. G. Wright, D. N. Christodoulides, and F. W. Wise, Opt. Lett. **41**, 3675 (2016).
38. A. Monmayrant, S. Weber, and B. Chatel, J. Phys. B **43**, 103001 (2010).
39. N. Coluccelli, M. Cassinerio, B. Redding, H. Cao, P. Laporta, and G. Galzerano, Nat. Commun. **7**, 12995 (2016).
40. B. Redding, S. F. Liew, Y. Bromberg, R. Sarma, and H. Cao, Optica **3**, 956 (2016).